REVIEW

LUMINESCENCE WILEY
The Journal of Biological and Chemical Luminescence

Recent advances in ZnO nanostructure as a gas-sensing element for an acetone sensor: a short review

Rajneesh Kumar Mishra[1] | **Vipin Kumar**[1] | **Le Gia Trung**[1] | **Gyu Jin Choi**[1] | **Jeong Won Ryu**[1] | **Rajesh Bhardwaj**[2] | **Pushpendra Kumar**[3] | **Jay Singh**[4] | **Seung Hee Lee**[5] | **Jin Seog Gwag**[1]

[1]Department of Physics, Yeungnam University, Gyeongsan, Gyeongbuk, South Korea

[2]Department of Physics, G.G.M. Science College (A Constituent College of Cluster University of Jammu), University of Jammu, Jammu & Kashmir, India

[3]Department of Physics, Manipal University Jaipur, Jaipur, Rajasthan, India

[4]Department of Chemistry, Institute of Science, Banaras Hindu University, Varanasi, U.P., India

[5]Department of Nanoconvergence Engineering and Department of Polymer Nano-Science and Technology, Jeonbuk National University, Jeonju, Jeonbuk, South Korea

Correspondence
Jin Seog Gwag, Department of Physics, Yeungnam University, Gyeongsan, Gyeongbuk, 38541, South Korea.
Email: sweat3000@ynu.ac.kr

Abstract

Air pollution is a severe concern globally as it disturbs the health conditions of living beings and the environment because of the discharge of acetone molecules. Metal oxide semiconductor (MOS) nanomaterials are crucial for developing efficient sensors because of their outstanding chemical and physical properties, empowering the inclusive developments in gas sensor productivity. This review presents the ZnO nanostructure state of the art and notable growth, and their structural, morphological, electronic, optical, and acetone-sensing properties. The key parameters, such as response, gas detection limit, sensitivity, reproducibility, response and recovery time, selectivity, and stability of the acetone sensor, have been discussed. Furthermore, gas-sensing mechanism models based on MOS for acetone sensing are reported and discussed. Finally, future possibilities and challenges for MOS (ZnO)-based gas sensors for acetone detection have also been explored.

KEYWORDS
acetone sensor, gas-sensing mechanisms, gas-sensing parameters, heterostructures/composites, ZnO

1 | INTRODUCTION

Recently, gas-sensing research has attracted significant attention towards volatile organic compounds (VOCs) due to their increasing air pollution and threats to human health.[1–3] Acetone has been recognized as the most promising research candidate among various VOCs for rapidly growing medical and industrial applications.[4] Acetone is the most toxic and pestiferous VOC among other gases, and causes irritation, coma, nausea, and vomiting.[5,6] Clinical reports have shown that healthy humans contain 300–900 ppb of acetone in their exhaled breath; however, a significant concern arises in diabetic patients if the concentration is above 1.8 ppm.[7] Also, high acetone concentrations affect the human central nervous system.[8]

Furthermore, exposure of the human body to acetone vapour over a long time causes severe health complications such as damage to the eyes and cardiovascular disease, chronic kidney disease, and stroke.[9,10] Therefore, there is an urgent demand for low-cost, swift, detectable, highly selective, and sensitive sensors to monitor and efficiently recognize acetone molecules for the safety and security of living objects.

Metal oxide semiconductors (MOS) are well known as a class of chemiresistive gas sensors that have had vast consideration for monitoring environmental pollution and food packaging safety testing due to their ease of use and inexpensive manufacture.[11–13] There are mainly two MOS-based chemical gas sensors: n-types, whose majority charge carriers are electrons, and p-types, in which holes play a

significant role in charge transport carriers, and which work mainly on the equilibrium change of the sensor's surface reaction with test gas molecules.[14–16] Zinc oxide (ZnO) is an n-type semiconducting material because of its native doping of oxygen vacancies. It is from the II–IV group family of semiconducting materials.[17] ZnO has evoked significant attention among various MOS nanostructures due to its excellent properties such as high colloidal stability, binding energy (exciton) of 60 meV, nontoxic and piezoelectric nature, high isoelectric points, pyroelectricity at room temperature, and so on.[18–23] Fascinatingly, ZnO has attracted enormous consideration because of its oxygen vacancy functions, which can also be utilized to fabricate oxygen sensors.[24] Interestingly, ZnO is a wide optical bandgap semiconducting material (3.37 eV) with a high free electron concentration of 10^{20} cm^{-3}.[25,26] ZnO exhibits a hexagonal wurtzite crystal phase related to the $P6_3mc$ space group and, therefore, O^{2-} ions are tetrahedrally integrated with four Zn^{2+} ions in the ZnO structure and vice versa.[27] ZnO has high electron mobility and mechanical and chemical stability.[28] Furthermore, the ZnO nanostructure is one of the most extensively studied MOS due to its outstanding physicochemical, physical, optical, electronic, and chemical properties, and so on.[29–33] Therefore, ZnO could be applicable for chemical gas sensors, SARS-CoV-2 sensing, NO_2 sensing, bio-sensor technologies, solar cells, biomedical nanotechnology, supercapacitors, memory devices, medicine, efficient delivery of curcumin to cancer, spintronic, electrochemical demonstration of vitamin C, optical waveguide sensors, TFTs, OLEDs, photocatalysts, and cancer therapy.[34–51] ZnO has been prepared as various types such as nanorod arrays,[52] quantum dots,[53] seed-like nanostructure,[54] nanosheets,[55] chrysanthemum-like nanostructure,[56] nanotubes,[57] 3D nanowalls,[58] and hexagonal nanostructure.[59] These nanostructural morphologies are extremely important for the performance of the ZnO-based acetone gas sensor. The ZnO nanostructure has been prepared using numerous synthesis methods such as spray pyrolysis,[60] solvothermal/hydrothermal methods,[61,62] sol–gel method,[63] electrodeposition method,[64] chemical vapour deposition (CVD),[65] chemical route,[66] magnetron sputtering method[67] and thermal evaporation method.[68]

This review covers the state of the art and noteworthy development in ZnO nanostructure morphological and structural properties for acetone gas-sensing applications. The influence of shape, size, and heterostructural engineering contributes significantly to the quick detection of acetone molecules from the workplace and environment. ZnO's electronic and optical properties and its nanocomposites have also been discussed. ZnO has intrinsic structural defects in zinc and oxygen vacancies, which can contribute significantly during gas sensing. Key parameters such as response, reproducibility, sensitivity, gas detection limit, selectivity, response and recovery time, and stability of the acetone sensor have been discussed. Furthermore, the review also explores sensing mechanisms, such as adsorption/desorption processes, the formation of active oxygen ions/sites on the ZnO sensor surface, and its interaction with the acetone molecules.

2 | STRUCTURAL, MORPHOLOGICAL, AND ELEMENTAL STUDIES

2.1 | Morphological study

N. Islavath has discussed the synthesis of a ZnO nanowall using a low-temperature hydrothermal method for 3 h at 95°C.[58] Figure 1(a–c) depicts the scanning electron microscopy (SEM) images of the ZnO nanowire, 3D nanowall, and hybrid 3D nanowall, and Figure 1(d–f) shows the corresponding cross-sectional view of SEM images of the ZnO nanowire, 3D nanowall, and hybrid 3D nanowall on the ZnO/Al–ZnO layer of seed-deposited fluorine-doped tin oxide (FTO) substrates. The ZnO nanowall formation depends entirely on the concentration of Al in the seed layer deposited on the FTO substrate, as shown in Figure 1(b and e, c and f). The thickness of the ZnO nanowall is measured as a length of 2 μm and width of nearly 20–25 nm using the cross-sectional SEM image in Figure 1(b, e). It is also discussed that as the Al concentration in the ZnO seed layer was increased, the 1D ZnO nanowires were transformed into 3D ZnO nanowalls, which resulted in an enhanced surface area. Additionally, the ZnO nanowalls were functionalized to nanowires, keeping the nanowall unaltered in thickness and length, as shown in Figure 1(c, f).

Alenezi and co-workers have studied the nucleation and growth of the various shapes and sizes of ZnO nanowires and ZnO nanodiscs using a hydrothermal method for gas-sensing applications.[69] Figure 2(a–h) shows the hierarchical ZnO structures taken from early 1D and 2D ZnO structures using a nucleation seed layer. Figure 2(a–c) depicts the SEM images of the hierarchical ZnO nanowires at different magnifications, which elucidates the self-assembly of nanowires to form a hexagonal symmetry. ZnO nanowires are expected to nurture around the surface of the core nanowire, which can be the leading cause for growing into a hexagonal symmetry. It was also observed that the core ZnO nanowire explored its six facets as the seed layer for forking the other nanowires onto it. Many researchers have studied similar reports in hexagonal-type symmetry.[70–73] The growth of ZnO nanowires on the facets of the ZnO core nanowire may be due to heterogeneous nucleation growth and low interfacial energy between the crystal nuclei and substrate, compared with the crystal nuclei and solutions. Here, the formation of hierarchical ZnO structures is possible with the help of 2D ZnO, ZnO nanodiscs, and ZnO nanotriangle. Figure 2(d, e) shows the top and side views of the single hierarchical ZnO nanodiscs. Figure 2(f) illustrates the high-magnification SEM image of the hierarchical ZnO nanotriangle. The above-discussed SEM images justified the growth of secondary nanowires on the core ZnO nanowire top, bottom, and sides. Figure 2(g) elucidates the growth direction of the ZnO nanowires in the [0001] direction, and the side surfaces are nonpolar planes. Figure 2(h) displays the high-magnification SEM image of the side view of several hierarchical ZnO nanodiscs, indicating highly densely populated and uniform ZnO nanowires grown on the core ZnO nanostructures.
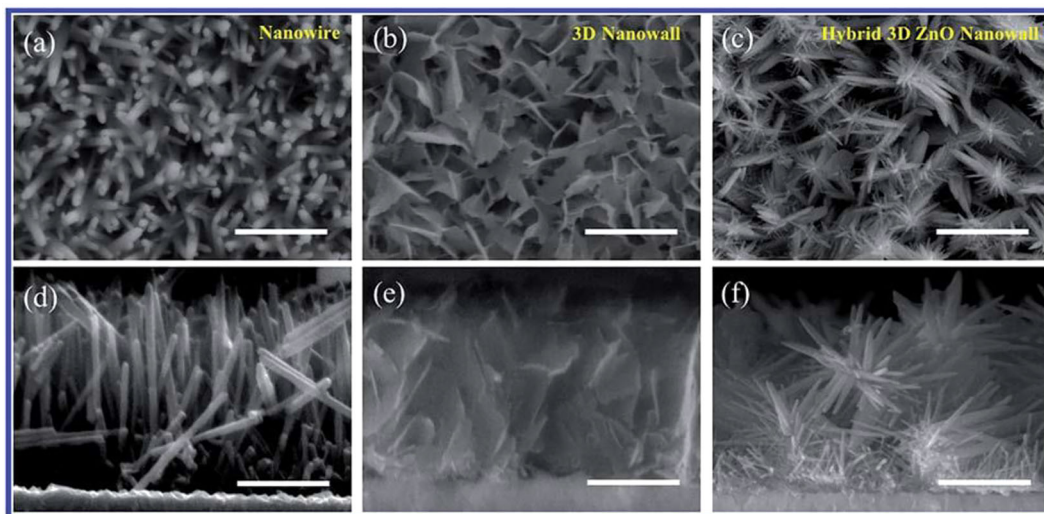
FIGURE 1 (a–c) SEM images of the ZnO nanowire, 3D nanowall, and hybrid 3D nanowall. (d–f) Corresponding cross-sectional view of SEM images of the ZnO nanowire, 3D nanowall, and hybrid 3D nanowall on the ZnO/Al–ZnO seed layer-coated FTO substrates. Scale bars, 2 μm. Reproduced with permission from ref. [58]. Copyright (2020) Royal Society of Chemistry

2.2 | Structural study

The ZnO nanostructure is a hexagonal wurtzite phase structure with lattice parameters of 3.251 Å (a = b) and 5.215 Å (c), which match well with JCPDS no. 36-1451.[74] Chen and co-workers discussed the ZnO nanoflower synthesis using the hydrothermal method.[75] Figure 3(a) illustrates the XRD spectra of the ZnO- and Au-doped ZnO nanoflowers of the hexagonal wurtzite crystal structure, which match well with JCPDS no. 36-1451.[76] The XRD diffraction peaks of the Au–ZnO nanoflowers are nearly identical to the bare ZnO nanoflowers. Furthermore, the Au concentration is not detected in the XRD spectra of Au–ZnO nanoflowers. This indicates a minimal amount of Au and low Au crystallinity in the Au–ZnO nanoflower composition. It is also seen that there were no impurity peaks in the ZnO and Au–ZnO nanoflowers. The calculated lattice parameters were 3.252 Å (a = b) and 5.209 Å (c) for ZnO; 3.251 Å (a = b) and 5.207 Å (c) for Au–ZnO W; 3.253 Å (a = b) and 5.210 Å (c) for Au–ZnO M; and 3.252 Å (a = b) and 5.209 Å (c) for Au–ZnO E. Moreover, the estimated lattice strains were 0.396 for ZnO, 0.369 for Au–ZnO-W, 0.421 for Au–ZnO M, and 0.431 for Au–ZnO E. The Au doping introduces a variation in the lattice parameters, which resulted in the presence of the lattice strain in the system.

Figure 3(b) displays the Raman vibrational phonon spectra of the ZnO and Au-doped ZnO nanoflowers.[77] Three prominent Raman vibrational phonon bands were observed at 436.4 cm^{-1}, corresponding to the characteristic E^{high}_2 mode. However, peaks at 331.3 cm^{-1} and 581.1 cm^{-1} were allocated to E^{high}_2 – E^{low}_2, and E_1(LO), respectively, of the second-order vibrational phonon modes. Therefore, these Raman vibrational phonon modes justify the formation of the hexagonal wurtzite structure of the ZnO nanoflowers. Lo and co-workers studied the ZnO nanostructure synthesis and Raman vibrational phonon modes using a two-step solution-processed method.[54]

The active Raman phonon bands of the ZnO structure were A_1 longitudinal optical (LO), A_1, E_1 transverse optical (TO), E_2(low), and E_2(high). It was also noted that E_2(high) was observed at 440 cm^{-1}, corresponding to the characteristics of the wurtzite phase. In addition, the strong E_2(high) Raman vibrational phonon band illustrated a highly crystalline nature. Furthermore, the Raman spectra peaks were broadened for large crystallite size distribution. Moreover, the E_1(TO) Raman mode showed the defective states such as interstitial zinc, oxygen vacancies, and their complexes. Using a two-step solution-process method, Damen and co-workers studied the ZnO nanostructure synthesis and Raman vibrational phonon modes.[77] The phonon E_2 vibrational modes were observed at 101 cm^{-1} and 437 cm^{-1}, the transverse mode A_1 at 381 cm^{-1}, transverse mode E_1 at 407 cm^{-1}, longitudinal mode A_1 at 574 cm^{-1}, and the longitudinal mode E_1 at 583 cm^{-1}.

Patil and co-workers studied the X-ray photoelectron spectroscopy (XPS) spectra of the ZnO films prepared using a hydrothermal method.[78] Figure 4(a) reveals the survey spectrum of the ZnO films with Zn 2p1, Zn 2p3, and O1s peaks, which showed the presence of zinc and oxygen elements. Figure 4(b) displays a narrow scan spectrum of Zn 2P of the ZnO nanostructure. The XPS peaks of Zn $2P_{3/2}$ and Zn $2P_{1/2}$ were observed at 1021.7 eV and 1044.8 eV, which belonged to the spin-orbit transition. Figure 4(c) displays a narrow scan spectrum of O1s of the ZnO nanostructure. The XPS peaks reported with the binding energies of 530.6 eV and 532.6 eV were allocated to O_2^- ions in the Zn-O and O^- and O^{2-} ions in the oxygen-deficient region. Similar XPS results for the ZnO nanostructure have been reported previously in the literature.[79–81]

Li and co-workers prepared ZnO nanoflowers using a hydrothermal method.[82] Figure 5(a) indicates a transmission electron microscopy (TEM) image of the ZnO nanoflower assembled with porous nanosheets. Figure 5(b) displays the high-resolution TEM (HRTEM)
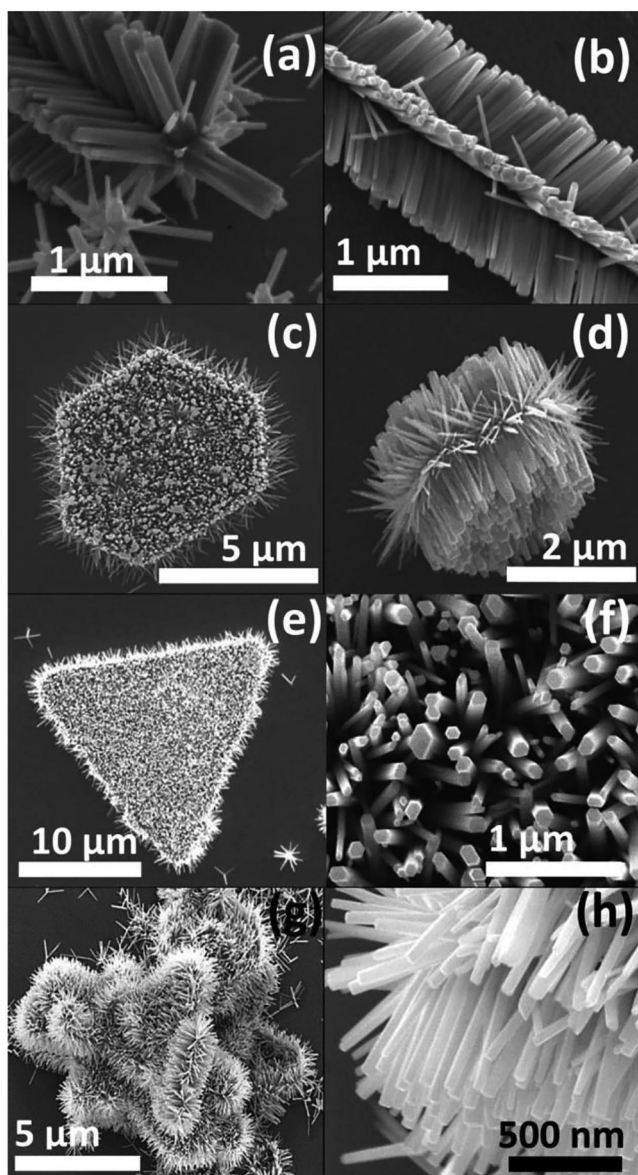
FIGURE 2 (a, b) Side view SEM images of hierarchical ZnO nanowires, (c) top, and (d) side view of single hierarchical ZnO nanodisc. (e) Top view of single hierarchical ZnO nanotriangle SEM image. (f) Top view of SEM image of ZnO nanowire grown on the core nanowire. (g) SEM image of single hierarchical ZnO nanodiscs. (h) Side view SEM image of the secondary nanowires on the hierarchical ZnO nanodiscs. Reproduced with permission from ref. [69]. Copyright (2014) Royal Society of Chemistry

image of the ZnO nanoflower corresponding to the (002) lattice plane, which shows the successful synthesis of the hexagonal wurtzite structure ZnO. Figure 5(c) indicates the corresponding selected area electron diffraction (SAED) pattern of the ZnO, which justified the HRTEM results and indicated the synthesis of the hexagonal wurtzite structure ZnO nanoflower. Figure 5(d–f) elucidates the high-angle annular dark field–scanning transmission electron microscope (HAADF-STEM) method and corresponding elemental mapping images of Zn and O elements from ZnO. Similar works have been studied and presented in the literature.[83,84]
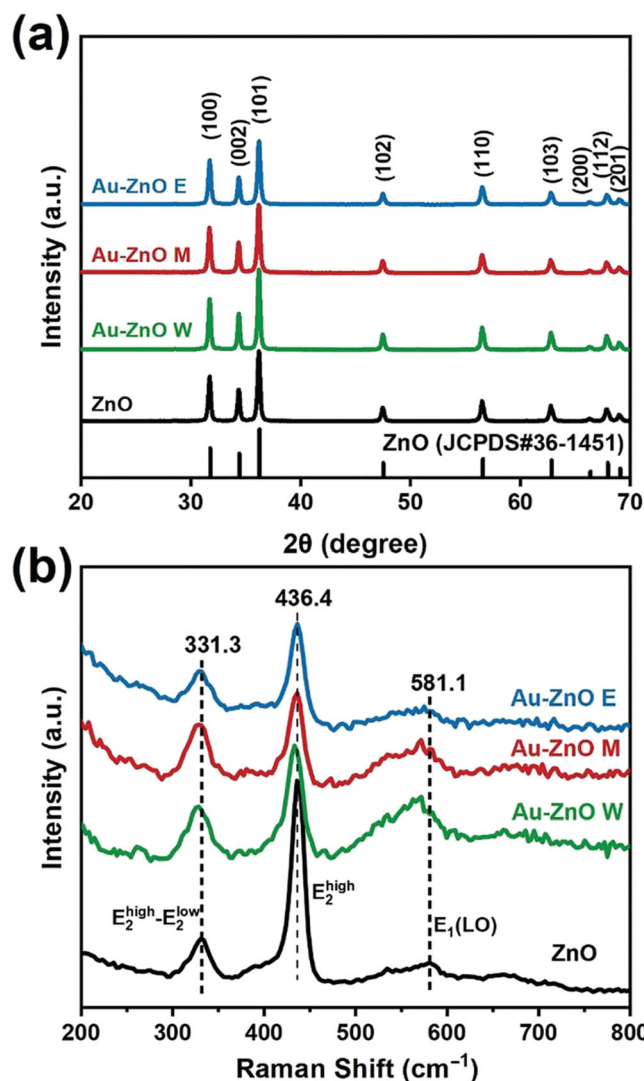

FIGURE 3 (a) XRD and (b) Raman spectra of the ZnO nanoflowers and Au–ZnO. Reproduced with permission from ref. [75]. Copyright (2021) Royal Society of Chemistry

3 | PROPERTIES OF ZnO NANOSTRUCTURE

3.1 | Electronic properties

The electronic properties of the ZnO nanostructure have been studied widely, theoretically, and experimentally for various applications. The electronic band structures of one-dimensional ZnO structures have been discussed using computational studies,[85] illustrating the wurtzite structure of ZnO with a direct bandgap of 0.72 eV. This theoretical bandgap (0.72 eV) is lower than the experimentally observed bandgap of 3.44 eV at 2 K. Marana, and co-workers investigated the electronic properties of the $(10\bar{1}0)$ and $(11\bar{2}0)$ surfaces of the ZnO nanostructure using density functional theory (DFT).[86] It was observed that the electronic bandgap of the $(10\bar{1}0)$ and $(11\bar{2}0)$ surfaces of the ZnO nanostructure were 2.85 eV and 3.09 eV,
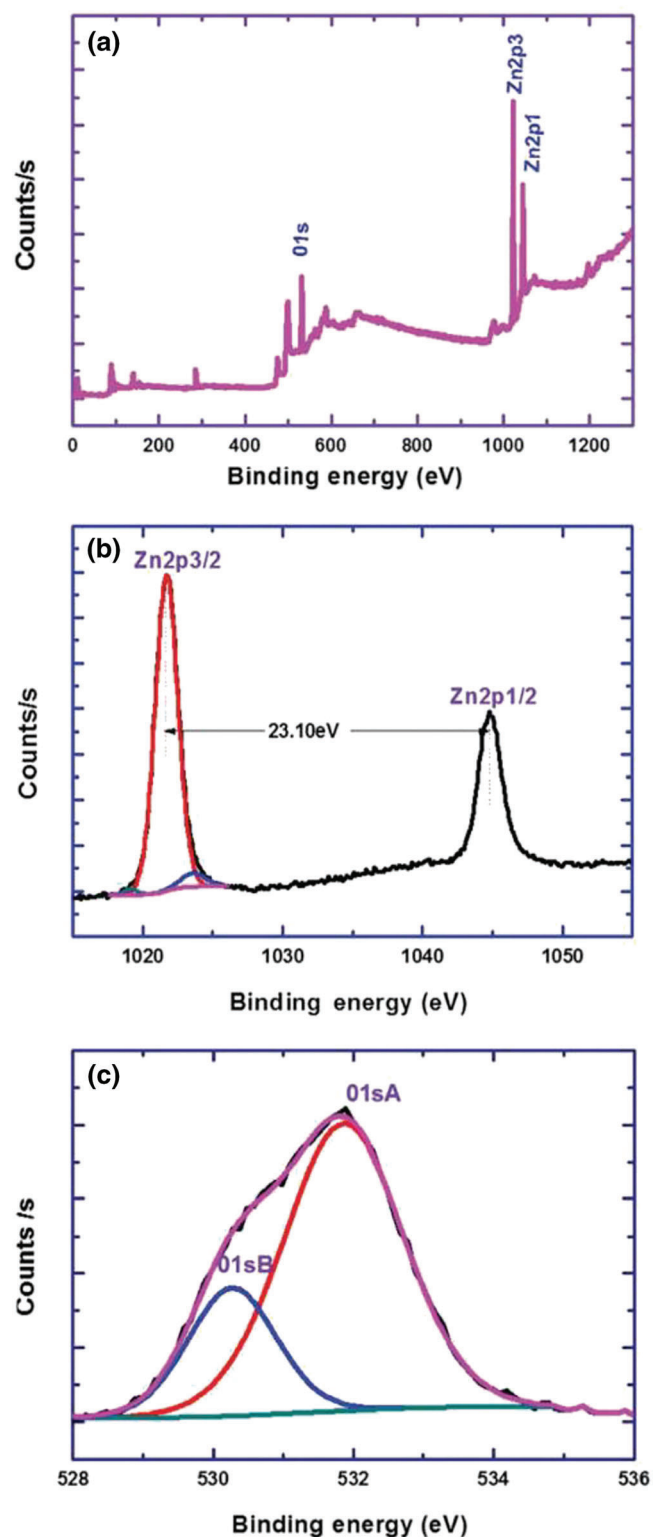
FIGURE 4 (a) Survey spectrum, (b) narrow scan spectrum of Zn 2p$_{3/2}$, and (c) narrow scan spectrum of O1s of the ZnO nanostructure. Reproduced with permission from ref. [78]. Copyright (2018) Royal Society of Chemistry

band for both surfaces of the ZnO nanostructure was observed at the Γ-point of the two-dimensional Brillouin zone. For the $(10\bar{1}0)$ surface, the valence band was achieved by the first and second layers of the zinc atom and the first layer of the oxygen atom, but the first layer of the zinc and oxygen atoms for the $(11\bar{2}0)$ surface. The electronic properties of the ZnO polymorph films have been studied and analyzed using the local density of states.[87] The engineering in the local density of states illustrated the decrease in the Madelung potential of the under-coordinated surfaces and atoms that appeared at the upper energy layer of the valence band and upper energy layer of the conduction band. Furthermore, quantum confinement was also observed because of the large energy gap width of the films compared with bulk. Xia and co-workers discussed different stacking configuration-engineered GaN/ZnO structures for their electronic and optical properties.[88] They showed that the stability and boding-type modulate with the stacking methods. Deep insights into the band structure of g-ZnO and g-GaN/g-ZnO have been discussed, and indicated the indirect bandgap for g-GaN and a direct bandgap of g-ZnO. It was observed from the projected density of states that the Zn-3d orbitals dominate the maximum of the valence band, whereas the minimum of the conduction band depends on Zn-4 s.

3.2 | Optical properties

The optical characteristics of the ZnO structure have been reported widely. The nanosized ZnO structure can give insights into the quantum confinement phenomena of electron–hole excitons.[89] The optical bandgap of the ZnO nanostructures was studied using the absorption spectra of liquid forms and reflectance spectra of the powder and thin films using ultraviolet–visible (UV–vis) light spectroscopy. The absorbance or diffuse reflectance results have been utilized to evaluate the optical bandgap of the MOS. The optical bandgap energies of the MOS were estimated using the Tauc relationship: $\alpha h v = A(h v - E_g)^k$, where A is the band-tailing parameter, α is the absorption coefficient, and k is 2 for indirect bandgap and 1/2 for direct bandgap semiconductors.[90,91] Moreover, the $(\alpha h v)^{1/k}$ versus $h v$ plots have been used to deduce the optical bandgap of the materials. The energy states related to the Urbach tail lying below the conduction band of the materials are well known as the Urbach energy states, which signifies the emergence of the defect states. The Urbach energy states can be assessed using the relationship: $\alpha = \alpha_o \exp(h v / E_u)$, where E_u is the Urbach energy, $h v$ is the photon energy, α is the absorption coefficient, and α_o is the constant.[91] In addition, using the diffuse reflectance spectra, the optical bandgap of the materials can also be estimated using the Kubelka–Munk function. The Kubelka–Munk function delivers the absorption coefficient value, which furthermore helps to evaluate the optical energy bandgap of the materials. The Kubelka–Munk function is written as; $F(R_\infty) = K/S = (1-R_\infty)^2 / 2 R_\infty$, where S is the scattering coefficient, R_∞ ($R_{sample}/R_{standard}$) is the diffuse reflectance of the infinitely thick specimen, and K is the absorption coefficient.[92] Furthermore, the optical energy bandgap can be estimated from the $[F(R_\infty) h v]^{1/n}$ versus $h v$ plots using the relationship: [F

respectively. It was illustrated that the upper part of the valance band for both the surfaces of the ZnO nanostructure was found to be coincident with the origin. Conversely, the lower part of the conduction
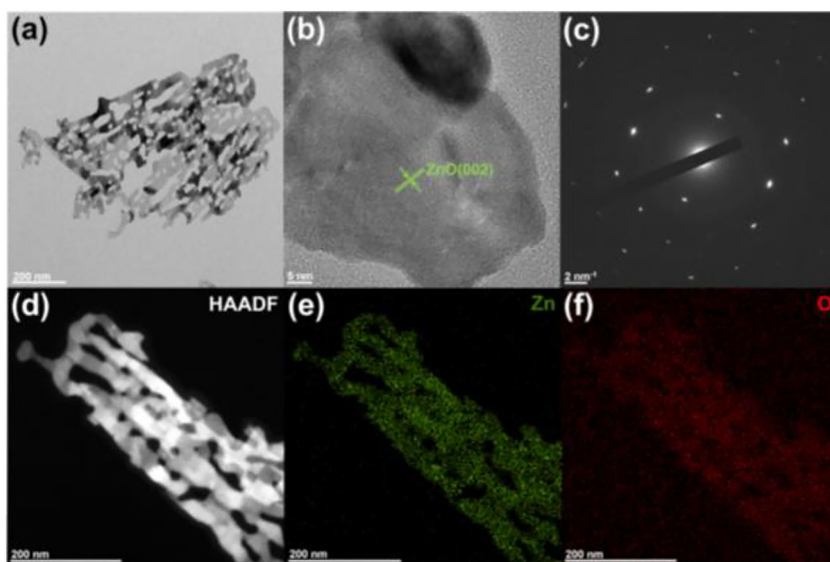
FIGURE 5 (a) TEM image, (b) HRTEM image, (c) SAED pattern, (d) HAADF image, and corresponding colour mapping of (e) Zn, and (f) O elements of the ZnO nanoflower. Reproduced with permission from ref. [82]. Copyright (2022) Elsevier
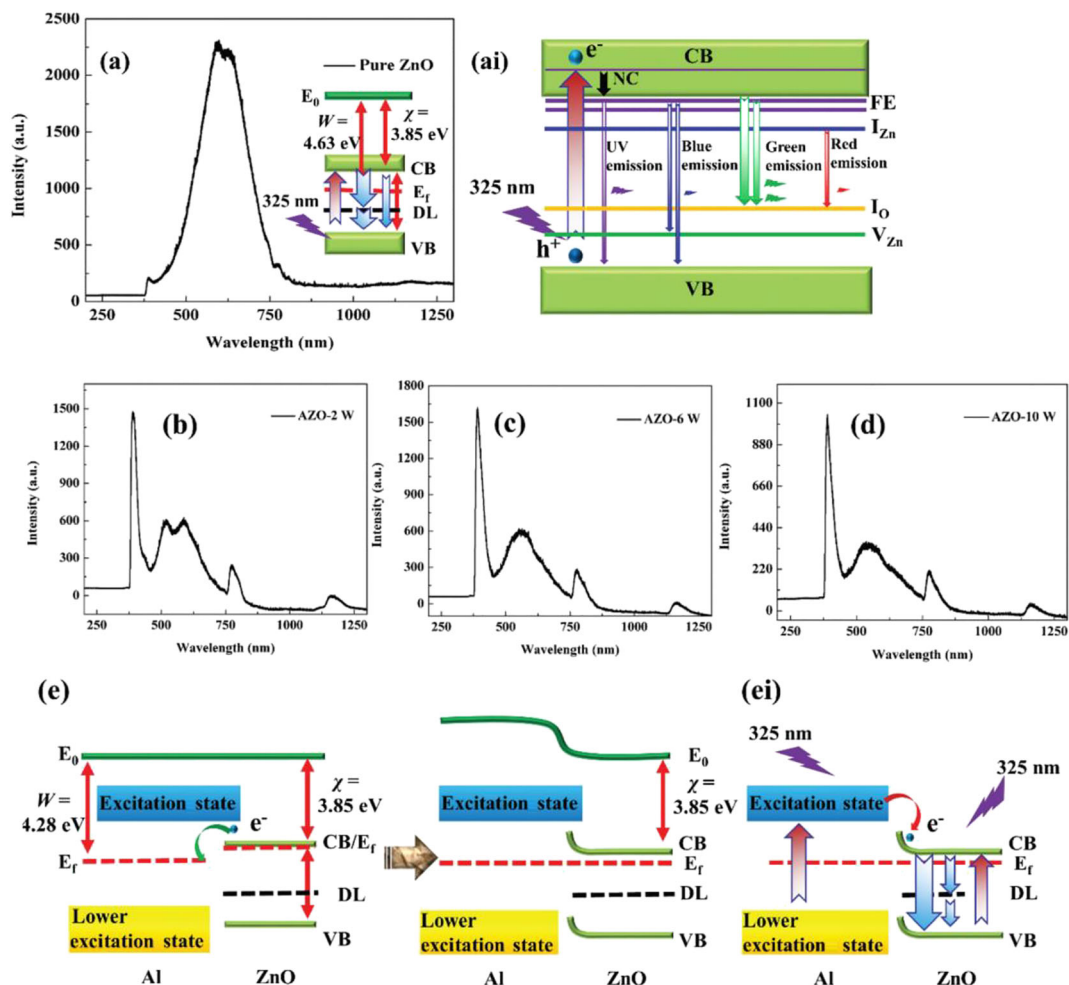

FIGURE 6 (a) PL spectrum of ZnO, (ai) illustration of electron transfer in ZnO band structure using the excitation wavelength of 325 nm. (b–d) PL spectra of Al-doped ZnO films. (e, ei) Schottky barrier and PL mechanism of the Al-doped ZnO (AZO) films. Reproduced with permission from ref. [96]. Copyright (2022) Royal Society of Chemistry

(R_∞) $h\nu] = C$ $(h\nu - E_g)^n$. The n values indicate whether the allowed transitions are direct for $n = 1/2$ or indirect for $n = 2$. The engineering of nanomaterial optical bandgap mainly depends on several factors such as doping, heterostructures, hybrids, and nanocomposites, which offer a wide variety of applications. The crucial role of Eu doping has been investigated to explore the electrical and optical properties of the ZnO nanostructure.[93] The upsurge in the optical bandgap of the ZnO structure with the growing concentration of Eu doping was observed. This can be due to the Burstein–Moss effect, which evolves from the degenerate doping of Eu in the ZnO nanostructure. Fascinatingly, ZnO exhibits intrinsic Zn, O vacancies, and interstitials, which play a crucial role in creating the defect energy states below the conduction band. The engineering in the optical properties and surface roughness of the ZnO nanostructure was noticed using the C ion implementation.[94] This showed a detected optical bandgap of 3.27 eV for C-60 and 3.20 eV for C-30. This may be because the presence of lattice strain/deformation leads to manoeuvring of the band edges, which causes the drive of the Fermi level towards the conduction band side. Furthermore, modulation in the optical bandgap of the ZnO was observed using silver (Ag) and graphene oxide (GO) as the dopants.[95] The optical bandgap of the Ag–GO-added ZnO nanocomposite was 2.75 eV, which is lower compared with the reported optical bandgap value of 3.37 eV.

The radiative and nonradiative transitions in the ZnO optical band were investigated by analyzing the emission spectra recorded using photoluminescence (PL) spectroscopy. Liu et al. studied the photoluminescence spectra of the ZnO structure and Al-doped ZnO (AZO) structure films using fluorescence spectroscopy, as revealed in Figure 6(a–ei).[96] Figure 6(a) explains the PL spectrum of the ZnO. It shows the free exciton recombination emission of ZnO near the band edge. It also suggests that the oxygen vacancy causes the defect states. Figure 6(ai) depicts the electron relocation from the upper energy layer of the valence band to the respective energy layers of the conduction band of ZnO using an excitation wavelength (325 nm) and radiative recombination emissions such as blue, green, and red. This process explains the existence of the defect states initiated by the interstitial Zn and oxygen vacancies. In addition, Figure 6(b–d) elucidates the PL spectra of the AZO structure films. The AZO films were observed to illuminate the weak emission at 468 nm because of the ionized oxygen vacancies created using Al^{3+}. They also exhibited green emission at 550 nm due to interstitial oxygen. Al-doping in the ZnO energizes AZO using lattice defects, producing the deep-level emission at 776.6 nm. Figure 6(e, ei) reveals the formation of the Schottky barrier and PL mechanism of the AZO films. This reveals the movement of electrons from the Fermi level of the ZnO to the Al atom. Therefore, this generates a higher potential barrier between the ZnO and Al, illustrating the formation of an n-type Schottky barrier. Therefore, it was concluded that the AZO films depicted more robust UV luminescence characteristics. Interestingly, the PL spectra of the RuO_2/ZnO hybrid were studied to explore radiative and nonradiative emissions.[97] This demonstrates that the PL radiative emission was enhanced in the visible region of 1.5–3.0 eV with the improved UV emission, where RuO_2 contributed a vital role. The PL spectra of ZnO and the graphene/ZnO hybrid were investigated to examine the radiative and nonradiative emissions.[98] It was observed that the graphene/ZnO hybrid illustrated low fluorescence yield compared with that of ZnO due to the mutual interactions between ZnO and graphene, which caused a reduction in charge carrier participation. PL spectroscopy results of In-doped ZnO showed different shapes such as nanotetrapods, nanowires, nanodisks, and nanocombs.[99] The nanotetrapods, nanowires, nanodisks, and nanocombs shapes of In-doped ZnO exhibited two radiative emission bands such as deep-level emission and near band edge (3.2 eV) emission. However, deep-level emissions were furthermore split into two bands, such as green and yellow, at 2.4 eV and 2.2 eV, respectively, because of the richness of oxygen vacancies. The richness of oxygen in the In-doped ZnO nanostructures may be due to the doping of trivalent indium cations. The PL spectra of Eu-doped ZnO have been studied to examine the crucial role of dopant (Eu) in the feasible radiative emissions using 325 nm excitation wavelength.[100] This illustrated the UV and green emissions at 396 nm and 515 nm, respectively. This may be because of the sallow donor arising from the structural defects of Zn, and oxygen vacancies arising during the deep-level to the valence band transition.[101] However, Eu^{2+} ions also generated an emission peak at 515 nm using the $4f^7–4f^65d^1$ transition. Therefore, it was concluded that ZnO with structural and morphological engineering can be a good candidate for photodiodes, photosensors, and several other desired optoelectronic devices.

4 | ACETONE-SENSING PERFORMANCES

Zhang and co-workers discussed the In/Ga oxide (IGO) nanotube sensor and IGO@ZnO sensor for acetone gas-sensing applications.[102] Figure 7(a) shows the acetone response versus operating temperature plots of the IGO nanotube sensor and IGO@ZnO sensor for 100 and 500 ppm acetone. It was found that the acetone response of the IGO@ZnO sensor increased and reached the maximum value of ~90 for a 500 ppm concentration. Furthermore, this decreased when increasing the temperature beyond 300°C. Similar trends were observed for all sensors at 100 ppm and 500 ppm. Figure 7(b) exhibits the transient characteristics of the IGO sensor and the IGO@ZnO sensor for different acetone concentrations at 300°C. It was observed that, as acetone concentration was increased, the response of the IGO@ZnO sensor increased quickly compared with the IGO sensor. The inset in Figure 7(b) illustrates the enlarged portion of the transient characteristics of the IGO sensor and the IGO@ZnO sensor for acetone concentration ranges of 200 ppb to 5 ppm at 300°C. The IGO@ZnO sensor detected the lowest acetone concentration of 200 ppb compared with the IGO sensor at 300°C. Figure 7(c) reveals a linear relationship in the response with the acetone gas concentration of the IGO sensor and the IGO@ZnO sensor at 300°C, which depicted the practical feasibility of identifying the acetone gas concentration quantitively. Figure 7(d) uncovers the estimation of response and recovery times of the IGO sensor and the IGO@ZnO sensor at 300°C. It was found that the IGO@ZnO sensor showed
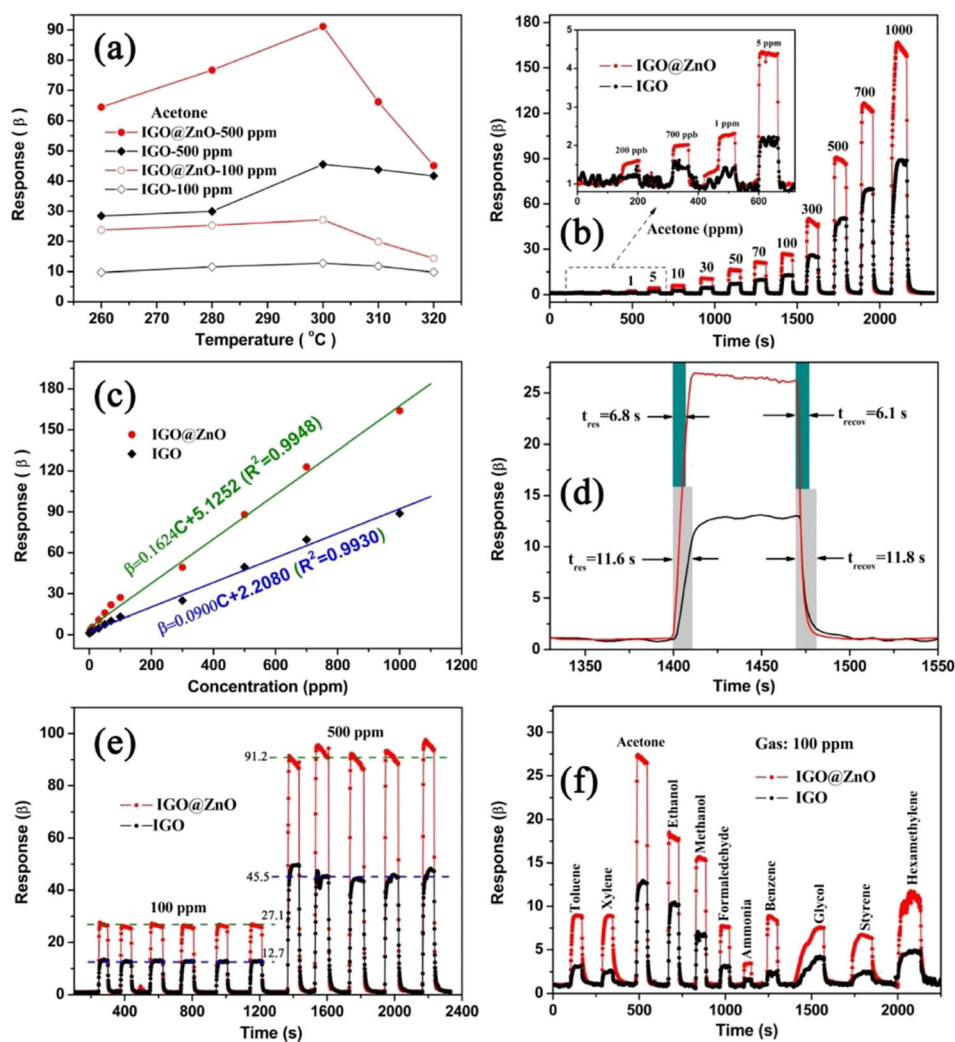
FIGURE 7 (a) Response vs. temperature plots of the IGO sensor and IGO@ZnO sensor with 100 and 500 ppm acetone. (b) Transient characteristics at various acetone concentrations at 300°C. (c) Response vs. acetone concentration plots at 300°C. (d) Calculation of response and recovery time for 100 ppm acetone concentration at 300°C. (e) Transient characteristics of IGO and IGO@ZnO with 100 and 500 ppm acetone at 300°C. (f) Selectivity plot of IGO and IGO@ZnO for 100 ppm at 300°C. Reproduced with permission from ref. [102]. Copyright (2020) American Chemical Society

times of the response (6.8 s) and recovery (6.1 s) for 100 ppm acetone at 300°C. However, the IGO sensor showed times of the response (11.6 s) and the recovery (11.8 s) for 100 ppm acetone at 300°C. Figure 7(e) unearths the transient characteristics of the IGO sensor and IGO@ZnO's transient characteristics for two different acetone concentrations of 100 ppm and 500 ppm at 300°C. It is perceived that the IGO@ZnO sensor discloses the quick and maximum response compared with the IGO sensor at 300°C. Figure 7(f) unearths the selectivity of the IGO sensor and IGO@ZnO's selectivity for 100 ppm concentrations of different interfering gases at 300°C. It was witnessed that the IGO@ZnO sensor depicts an excellent response to acetone gas compared with other interfering gases for the 100 ppm concentration at 300°C. Brahma and co-workers studied the acetone sensor based on Cu-doped p-type ZnO nanostructures.[103] It was detected that the 1.1 at% Cu-doped p-type ZnO showed excellent acetone-sensing properties even at a minimal concentration of 1 ppm at room temperature. Here, Cu doping contributed a significant role in tuning the electronic properties of ZnO. Qi and co-workers investigated the selectivity of acetone sensors based on ZnO nanostructure.[104] It was observed that the ZnO nanostructure shows a high response of ~180, a fast response time of 1.5 s, and a recovery time

of 3 s at 300°C. In addition, the preadsorbed O_2 on the surface of the ZnO nanostructures can also play a key role in acetone detection, as discussed theoretically and experimentally by C. Li and co-workers.[105] They studied the DFT calculation of the presence of O_2 molecules on the (001) facet of the ZnO to examine the acetone-sensing behaviour. The ZnO sensor illustrated a response time of 8 s and a recovery time of 50 s for 1000 ppm at 105°C. It exhibited outstanding selectivity and stability for 1000 ppm of acetone at 105°C. The acetone gas detection can also be influenced using the $ZnFe_2O_4$ nanoparticles grown on the ZnO surface, as discussed by Y. Song and co-workers.[106] The ZnFe2O4/ZnO sensor was perceived to reveal an outstanding response of 225 ± 15 and a quick response (6 s) for 100 ppm at 260°C. It was also analyzed that the n–n junction $ZnFe_2O_4$/ZnO could produce more active sites on the sensor surface because of the large number of free electrons and could also be a primary factor for enhanced acetone response. Functionalization can also play an essential role in the ppb level acetone detection. D. Liu and co-workers studied the Fe-functionalized α-Fe_2O_3/ZnO nanocages for acetone gas recognition at ppb concentration.[107] They illustrated a response of 45.3, a response (recovery) time of 7 s (6 s), and a low acetone detection limit (500 ppb) of

the Fe-functionalized α-Fe$_2$O$_3$/ZnO sensor. P. Wang and co-workers reported on the Au-functionalized ZnO nanostructure to investigate acetone-sensing behaviour.[108] HSs-3 showed excellent acetone sensing for a 100 ppm concentration at 365°C. It also depicted a fast response time of 5 s and a good acetone selectivity at 100 ppm and 365°C. In addition, the nanofibre morphology and oxygen-plasma-assisted ZnO played a significant role in the improved and quick response to acetone molecules detection. H. Du and co-workers investigated the theoretical and experimental oxygen-plasma-assisted acetone detection of the ZnO nanofibre-based sensor.[109] The oxygen-plasma-assisted ZnO exhibited the highest response compared with hydrogen-plasma-assisted ZnO and untreated ZnO-based sensors. The oxygen-plasma-assisted ZnO sensor elucidated a fast response time (75 s), quick recovery (125 s), excellent repeatability, and selectivity. Interestingly, MOS/MOS heterostructures were studied to enhance the detection of acetone molecules at low temperatures and concentrations. J. E. Lee and co-workers investigated acetone detection at the ppb level using ZnO–CuO nanostructures.[110] This showed the lowest acetone detection limit of 9 ppb; however, the response can be recorded up to 40 ppb acetone concentration. This showed high stability over 40 days and good selectivity for a 1 ppm acetone concentration at 200°C.

5 | KEY SENSOR PARAMETERS

The following vital factors determine the gas recognition properties of the chemical gas sensor.

5.1 | Concentration

The concentration of test gas (liquid) can be calculated using the following Equation (1)[111–113]:

$$C\,(ppm) = \frac{22.4 \times d \times \rho \times V_x}{V \times M} \times 10^3 \qquad (1)$$

where C, d, ρ (g ml^{-1}), V_x (μl), V (L), and M (g mol^{-1}) are the concentration of the test gas, gas volume fraction, liquid density, the volume of the liquid test gas, the volume of the gas testing chamber, and the molecular mass of the liquid test gas, respectively.

5.2 | Response

The response is clarified as the percentage change in sensor resistance in the air and during the test gas inside the gas-sensing measurements chamber. The response is written for reducing and oxidizing gases using the following Equations (2) for reducing gas and (3) for oxidizing gas[114–116]:

$$\text{Response}\,(\%) = \frac{R_a - R_g}{R_a} \times 100 \;\;[\text{Reducing gas}] \qquad (2)$$

$$\text{Response}\,(\%) = \frac{R_g - R_a}{R_a} \times 100 \;\;[\text{Oxidizing gas}] \qquad (3)$$

where R_g is the sensor resistance in the gas and R_a is the sensor resistance in the air.

Furthermore, in some studies, the response was interpreted as the ratio between the sensor element's resistance in air and during the test gas. Therefore, the response is written for reducing and oxidizing gases using the following Equations (4) for reducing gas and (5) for oxidizing gas[116,117]:

$$\text{Response} = \frac{R_a}{R_g} \;\;[\text{Reducing gas}] \qquad (4)$$

$$\text{Response} = \frac{R_g}{R_a} \;\;[\text{Oxidizing gas}] \qquad (5)$$

5.3 | Sensitivity

Sensitivity explains the ability of the chemical gas sensor to distinguish minute variances in the concentration of the test gas during an investigation. Therefore, high sensitivity means the high efficiency of the gas sensor. The sensitivity of the test gas can be defined as the following Equation (6)[118]:

$$\text{Sensitivity} = \frac{Test\,gas\,response}{test\,gas\,concentration} \qquad (6)$$

5.4 | Response and recovery time

Response and recovery allude to the reversibility of the test gas molecule desorption and adsorption reaction rate on the sensor surface at a specific concentration and temperature. Response and recovery times are significant in evaluating the sensitive behaviour of the gas-sensing nanomaterial element in the gas sensor.[119] The response time elucidates the time the gas sensor takes to reach 90% of the top response after inserting the test gas into the gas chamber.[111] However, the recovery time divulges the time observed using the gas sensor to touch 90% of its initial value after no coverage of test gas.[120] The fast response and recovery are indispensable for the gas sensor's better performance.

5.5 | Gas detection limit

The gas detection limit highlights the lowest detection gas concentration to differentiate the gas signal from the noise signal of the

gas-sensor device.[121] The observed value of the detection limit of sensor response should be several times higher than the noise signal.[122] The gas sensor's detection limit (DL) is the exclusive parameter to discriminate the lowest limit of the particular gas during the gas test. The DL can be evaluated using the following Equations (7) and (8)[123–125]:

$$DL = 3\frac{rms_{noise}}{S} \tag{7}$$

where S is the slope of the logarithmic plot between gas response versus gas concentration and rms_{noise} is the root-mean-square deviation from the baseline and is defined by the following Equation (8)[123–125]:

$$rms_{noise} = \sqrt{\frac{\sum (x - x_i)^2}{P}} \tag{8}$$

where x, x_i, and P are the baseline data points, the average value of baseline data points, and the number of data points, respectively.

5.6 | Reproducibility

Reproducibility validates the steadiness in the gas response at a particular concentration and temperature of the sensor over its repetitive use of service. This also suggests the working life of the particular gas sensor, meaningfully decreasing the installation cost of the fabrication and operation of the gas sensor in industrial or residential areas.

5.7 | Selectivity

Selectivity is a significant parameter for identifying the gas from the gas clusters at a fixed concentration and operating temperature. The selectivity coefficient (SC) of the test gas can be evaluated quantitatively concerning the other interfering gases using the following Equation (9)[126,127]:

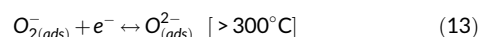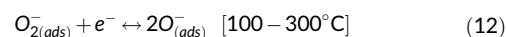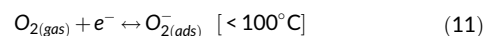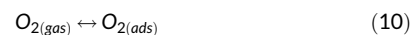$$SC = \frac{S_{test\ gas}}{S_{interfering\ gas}} \tag{9}$$

where $S_{test\ gas}$ and $S_{interfering\ gas}$ represent the particular response of the test gas and response to the respective interfering gases. The gas sensor device's high gas SC indicates the sensor's transient and selective nature for the particular gas. Therefore, improving the SC of the sensor by engineering the gas-sensing nanomaterial element has attracted significant attention and has become a great concern in recent research fields.

5.8 | Stability

The stability of the gas sensor is also a vital parameter to examine the practical and commercial applications. Stability elucidates the gas-sensing test over a long time to recognize the consistency of the gas sensor device without lowering the response.[128] Furthermore, stability is interpreted as the capability of the gas sensor device to conserve response, sensitivity, and selectivity over a long time.[129] Therefore, these above-discussed factors, such as test gas concentration, operating temperature, response and recovery time, sensitivity, gas DL, selectivity, reproducibility, and stability, play crucial roles in determining the efficiency and productivity of the gas sensors.

6 | ACETONE-SENSING MECHANISM

The acetone-sensing mechanism of the sensor device typically depends on the changes in resistance under the exposure of the test gas because of the chemisorption process between the adsorbed oxygen species and the gas molecules on the sensor surface.[130,131] It is recognized that the response and recovery of the gas sensor rely on the interactions between the test gas molecule species and adsorbed oxygen ions/sites on the surface of the gas sensor element.[13] However, the adsorbed oxygen ions/sites are unhesitatingly dependent on the working temperature of the gas sensor device, which can be written as follows in Equations (10)–(13)[131–135]:

$$O_{2(gas)} \leftrightarrow O_{2(ads)} \tag{10}$$

$$O_{2(gas)} + e^- \leftrightarrow O_{2(ads)}^- \quad [<100°C] \tag{11}$$

$$O_{2(ads)}^- + e^- \leftrightarrow 2O_{(ads)}^- \quad [100-300°C] \tag{12}$$

$$O_{2(ads)}^- + e^- \leftrightarrow O_{(ads)}^{2-} \quad [>300°C] \tag{13}$$

Equations (10)–(13) demonstrate the active ion oxygen species formation in the gas sensor's working temperature ranges. First, the atmospheric oxygen is adsorbed on the surface of the acetone gas sensor [Equation 10]. After that, adsorbed oxygen interacts with the electrons of the conduction band that are thermally excited from the valence band, resulting in the creation of active oxygen ions/sites of $O_{2(ads)}^-$ on the sensor surface, as discussed in Equation (11). Furthermore, this active oxygen ion species of $O_{2(ads)}^-$ again interacts with the conduction band electrons to form the active oxygen ion species of $O_{(ads)}^{2-}$ on the sensor surface, as shown in Equation (13). Furthermore, the chemisorption of acetone molecules with active oxygen ions/sites on the gas sensor surface is written as follows in Equations (14) and (15)[136,137]:
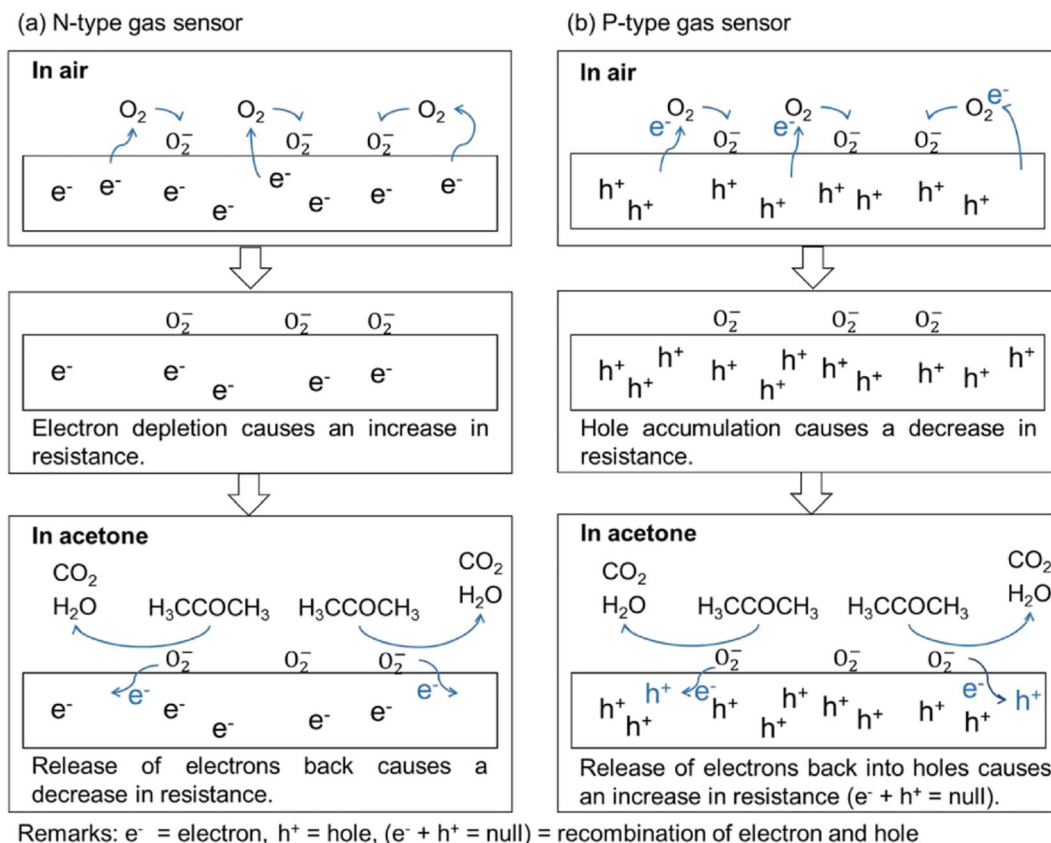
$$CH_3COCH_{3(ads)} + 8O_{(ads)}^- \rightarrow 3CO_2 + 3H_2O + 8e^- \quad [100-300°C] \tag{14}$$
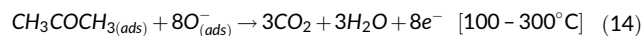
FIGURE 8 (a) Interaction of atmospheric oxygen with the n-type gas-sensing material's surface to form the active oxygen ion species and after interactions of these active oxygen ion species with acetone molecules. Similarly (b) formation of active oxygen ion species and their interaction with the p-type gas-sensing material's surface. Reproduced with permission from ref. [138]. Copyright (2019) Elsevier

$$CH_3COCH_{3(ads)} + 8O^{2-}_{(ads)} \rightarrow 3CO_2 + 3H_2O + 16e^- \quad [>300°C] \quad (15)$$
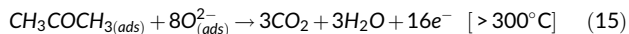
Here, acetone molecules interact with the active oxygen species (O^-) at the working temperature of 100–300°C of the gas sensor device, which separates acetone molecules into carbon dioxide, and water molecules, and releases electrons into the conduction band of gas-sensing materials, as discussed in Equation (14). In addition, the interactions of the acetone molecules with the active oxygen species (O^{2-}) at the temperature of >300°C of the gas sensor device suggest the liberation of carbon dioxide and water molecules, and discharge of electrons into the conduction band of the gas-sensing materials, as discussed in Equation (15).

Furthermore, Baharuddin and co-workers studied the schematic illustration of the formation of active oxygen ion species and their interactions with the acetone molecules for n-type and p-type gas sensor devices, as explored in Figure 8(a, b).[138] Figure 8(a) illustrates the formation of the O_2^- active oxygen ions/sites on the gas sensor surface via adsorption and interaction of oxygen O_2 with the thermally excited conduction electron of the n-type gas-sensing materials, as discussed in Equations (10)–(13). Therefore, this indicates the construction of the electron-depletion region near the sensor surface of the gas-sensing material, which causes an increase in the gas sensor device resistance. Furthermore, the interaction of the active oxygen

species (O_2^-) with the acetone target gas molecules results in carbon dioxide gas, water molecules, and the liberation of electrons back to the conduction band, as discussed in Equations (14) and (15). Similarly, Figure 8(b) shows the formation of O_2^- active oxygen ion species on the gas sensor surface via adsorption and interaction of atmospheric oxygen O_2 with the conduction holes of the p-type gas-sensing materials. Therefore, this indicates the formation of the hole accumulation region near the surface of the p-type gas-sensing material, which causes a decline in the sensor device resistance. In addition, the interaction of the active oxygen species (O_2^-) with the acetone target gas molecules results in the evolution of carbon dioxide gas and water molecules and the liberation of holes into the conduction band of the gas-sensing materials.

Moreover, Wang and co-workers elucidated the schematic representation of the formation, adsorption, and desorption and interaction of active oxygen ions/sites with the acetone molecules on the CuO–ZnO hetero-junction-based gas sensor surface, as shown in Figure 9.[139] It was observed that active oxygen species formation and their interaction with the acetone molecules are not identical to the ZnO/rGO nanocomposite because of the development of the p–n junction CuO–ZnO. In steps 1 and 2, the adsorption of atmospheric oxygen and their conversion into active oxygen species (O_2^-), as discussed in Equations (10) and (11), causes the formation of the first
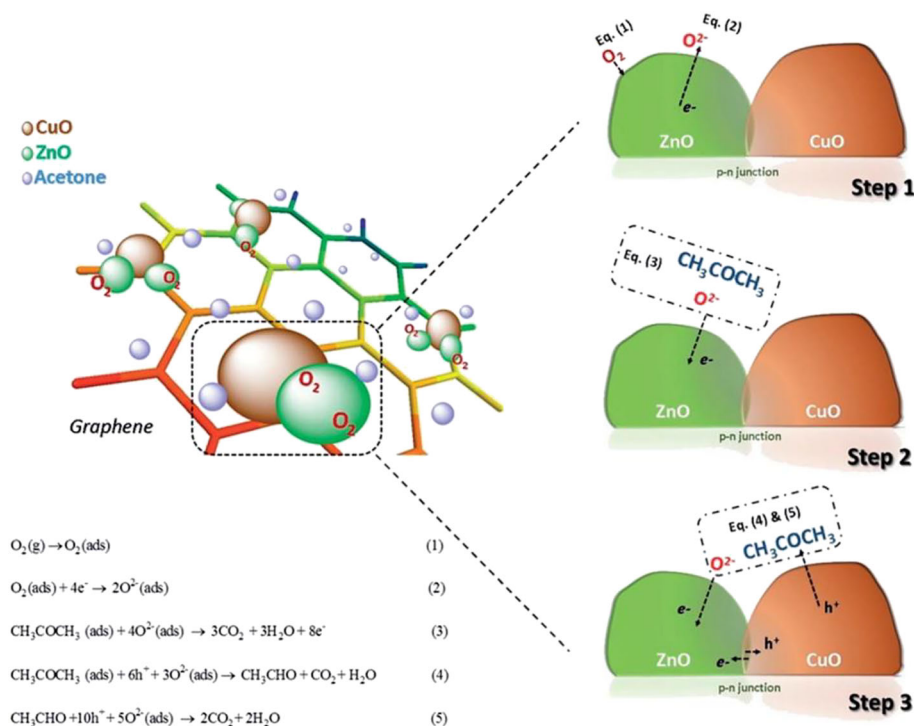
FIGURE 9 Schematic illustration of the p–n junction CuO–ZnO@RGO nanostructure. Reproduced with permission from ref. [139]. Copyright (2014) Royal Society of Chemistry

$$O_2(g) \rightarrow O_2(ads) \tag{1}$$

$$O_2(ads) + 4e^- \rightarrow 2O^{2-}(ads) \tag{2}$$

$$CH_3COCH_3(ads) + 4O^{2-}(ads) \rightarrow 3CO_2 + 3H_2O + 8e^- \tag{3}$$

$$CH_3COCH_3(ads) + 6h^+ + 3O^{2-}(ads) \rightarrow CH_3CHO + CO_2 + H_2O \tag{4}$$

$$CH_3CHO + 10h^+ + 5O^{2-}(ads) \rightarrow 2CO_2 + 2H_2O \tag{5}$$

depletion region at the surface of ZnO. Subsequently, the second depletion region was formed on the surface of the CuO–ZnO heterojunction. Furthermore, the interaction of acetone molecules with O^{2-} on the n-type ZnO surface is discussed in Equation (13). However, for the p–n CuO–ZnO heterojunction, the adsorbed atmospheric oxygen reacts with the electrons and holes of the n-type ZnO and p-type CuO to form the adsorbed active oxygen (O^{2-}), as discussed in Equations (10)–(13) and step 3. After that, the interaction of O^{2-} with the acetone molecules shows an enhanced and quick response. The p-type CuO nanostructure in the CuO–ZnO heterojunction starts to transfer charges from bulk to adsorbed gas molecules.[140] It was also reported that the conduction band edge of CuO was greater than the ZnO in the CuO–ZnO heterojunction; therefore there was movement of electrons towards the conduction band of ZnO from CuO. However, the hole migrates in the opposite direction from the valence band of ZnO to CuO, which results in the accumulation of more electrons in the conduction band of ZnO.[141,142] Additionally, Lv and coworkers discussed mechanisms for the formation of active oxygen species (in the temperature ranges <100°C, 100–300°C, and >300°C) on the surface of the $ZnFe_2O_4$ sensor.[143] The reaction mechanism and interactions of adsorbed O^- active oxygen ions/sites with molecules of acetone on the surface of the $ZnFe_2O_4$ sensor have also been discussed.

7 | FUTURE POSSIBILITIES AND CHALLENGES

This short review summarizes metal oxide semiconductor-based gas sensor device morphologies, crystal structure, electronic and optical properties, vital influencing parameters, and gas-sensing mechanisms.

Moreover, we evaluated the ZnO sensor's future possibilities, merits, and challenges for acetone gas-sensing applications. The formation of heterostructures, elemental doping, and defects are crucial for engineering the band structure and amending the transport, optical, and electronic properties to improve gas-sensing applications and enhance sensitivity, stability, and selectivity. Furthermore, the ZnO nanostructure has high adsorption energy, improving the gas sensor's quick detection and selective nature. The modulation of the physisorption and chemisorption process can also tune the ZnO sensor's fast response and recovery time. The formation of the p–n-type heterojunctions and nanocomposite with carbon nanomaterials of the ZnO gas-sensing element is favourable for high sensitivity, quick response, low DL, and fast recovery of the gas sensor. However, it is still not as low as an essential DL for portable biomarker detection. For high selectivity, there is also a need to optimize the sensor's working conditions under high humidity conditions because of the human's saturated moisture in exhaled breath. Therefore, new heterostructures with nanograins, nanorods, core-shell, nanowires, etc., of the ZnO semiconductor can contribute to a substantial role in overcoming the limitations of the acetone sensor. In addition, matching the gas-sensing material element's work function and band energy with the working sensing material for producing compelling and sensitive gas sensors is exceptionally desirable. Therefore, it was concluded that developing new heterostructure materials with engineered nanostructures could enhance the overall performance of the gas sensor.

ORCID

Rajneesh Kumar Mishra https://orcid.org/0000-0001-9634-354X

Vipin Kumar https://orcid.org/0000-0002-2211-2607

Pushpendra Kumar https://orcid.org/0000-0002-4435-1430

Jay Singh https://orcid.org/0000-0002-3793-0450

REFERENCES

[1] C. Liu, L. Zhao, B. Wang, P. Sun, Q. Wang, Y. Gao, X. Liang, T. Zhang, G. Lu, *J. Colloid Interface Sci.* **2017**, *495*, 207.

[2] T. Xiao, X.-Y. Wang, Z.-H. Zhao, L. Li, L. Zhang, H.-C. Yao, J.-S. Wang, Z.-J. Li, *Sens. Actuators B* **2014**, *199*, 210.

[3] R. Bhardwaj, A. Hazra, *J. Mater. Chem. C* **2021**, *9*, 15735.

[4] W. Liu, L. Xu, K. Sheng, X. Zhou, B. Dong, G. Lu, H. Song, *NPG Asia Mater.* **2018**, *10*, 293.

[5] C. Xue, Y. Zhang, B. Liu, S. Gao, H. Yang, P. Li, N. D. Hoa, Y. Xu, Z. Zhang, J. Niu, X. Liao, D. Cui, H. Jin, *ACS Sens.* **2022**, *7*, 1581.

[6] E. Wongrat, N. Chanlek, C. Chueaiarrom, W. Thupthimchun, B. Samransuksamer, S. Choopun, *Ceram. Int.* **2017**, *43*, S557.

[7] W.-N. Zhao, N. Yun, Z.-H. Dai, Y.-F. Li, *RSC Adv.* **2020**, *10*, 1261.

[8] M. M. Rahman, M. M. Alam, A. M. Asiri, *New J. Chem.* **2017**, *41*, 9938.

[9] L. Cai, X. Dong, G. Wu, J. Sun, N. Chen, H. Wei, S. Zhu, Q. Tian, X. Wang, Q. Jing, P. Li, B. Liu, *Sens. Actuators B* **2022**, *351*, 130863.

[10] Y. Xiong, X. Chang, X. Qiao, K. Li, L. Zhu, F. Xia, X. Li, Q. Zheng, W. Xing, Q. Xue, *Sens. Actuators B* **2019**, *300*, 127011.

[11] S. M. Majhi, A. Mirzaei, S. Navale, H. W. Kim, S. S. Kim, *Nanoscale* **2021**, *13*, 4728.

[12] L. Chen, Z. Liu, Z. Guo, X.-J. Huang, *J. Mater. Chem. A* **2020**, *8*, 17326.

[13] Y. Cheng, B. Ren, K. Xu, I. Jeerapan, H. Chen, Z. Li, J. Z. Ou, *J. Mater. Chem. C* **2021**, *9*, 3026.

[14] S. Shao, H. Wu, S. Wang, Q. Hong, R. Koehn, T. Wu, W.-F. Rao, *J. Mater. Chem. C* **2015**, *3*, 10819.

[15] C. H. Cho, J. Y. Oh, T. I. Lee, *Mater. Lett.* **2022**, *314*, 131826.

[16] F. Wang, H. Li, Z. Yuan, Y. Sun, F. Chang, H. Deng, L. Xie, H. Li, *RSC Adv.* **2016**, *6*, 79343.

[17] S. Raha, M. Ahmaruzzaman, *Nanoscale Adv.* **2022**, *4*, 1868.

[18] W. Lee, J. Yeop, J. Heo, Y. J. Yoon, S. Y. Park, J. Jeong, Y. S. Shin, J. W. Kim, N. G. An, D. S. Kim, J. Park, J. Y. Kim, *Sci. Rep.* **2020**, *10*, 18055.

[19] Y. Q. Su, Y. Zhu, D. Yong, M. Chen, L. Su, A. Chen, Y. Wu, B. Pan, Z. Tang, *J. Phys. Chem. Lett.* **2016**, *7*, 1484.

[20] M. Jin, N. Li, W. Sheng, X. Ji, X. Liang, B. Kong, P. Yin, Y. Li, X. Zhang, K. Liu, *Environ. Int.* **2021**, *146*, 106179.

[21] H. Gullapalli, V. S. M. Vemuru, A. Kumar, A. B. Mendez, R. Vajtai, M. Terrones, S. Nagarajaiah, P. M. Ajayan, *Small* **2010**, *6*, 1641.

[22] C. S. Lim, *J. Ceram. Process. Res.* **2010**, *11*, 631.

[23] C. S. Wei, Y. Y. Lin, Y. C. Hu, C. W. Wu, C. K. Shih, C. T. Huang, S. H. Chang, *Sens. Actuators, a* **2006**, *128*, 18.

[24] N. Verma, M. Rakhra, M. W. Bhatt, U. Garg, *Neurosci. Informatics* **2022**, *2*, 100015.

[25] M. Kolaei, M. Tayebi, Z. Masoumi, B.-K. Lee, *J. Alloys Compd.* **2022**, *906*, 164314.

[26] N. Nosidlak, J. Jaglarz, P. Dulian, R. Pietruszka, B. S. Witkowski, M. Godlewski, W. Powroźnik, T. Stapiński, *J. Alloys Compd.* **2022**, *900*, 163313.

[27] B. O. Casas, A. G. Martínez, J. G. Flores, A. B. Ibáñez, P. K. Panda, G. Santana, H. A. de la Vega, M. Suar, C. G. Rodelo, A. Kaushik, Y. K. Mishra, A. Dutt, *Mater. Today* **2021**, *50*, 533.

[28] P. Rai, Y.-S. Kim, H.-M. Song, M.-K. Song, Y.-T. Yu, *Sens. Actuators B* **2012**, *165*, 133.

[29] A. Guleria, M. K. Meher, N. Prasad, K. M. Poluri, D. Kumar, *J. Phys. Chem. C* **2017**, *121*, 18598.

[30] N. Hamzaoui, A. Boukhachem, M. Ghamnia, C. Fauquet, *Results Phys.* **2017**, *7*, 1950.

[31] M. Kahouli, A. Barhoumi, A. Bouzid, A. A. Hajry, S. Guermazi, *Superlattices Microstruct.* **2015**, *85*, 7.

[32] Y. Miao, Z. Wang, H. Zhao, Q. Chen, H. Wang, M. Wan, L. Chen, K. He, Q. Wang, *Mater. Sci. Eng., B* **2020**, *254*, 114517.

[33] W. Tu, C. Sun, Z. Zhang, W. Liu, H. S. Malhi, W. Ma, M. Zhu, Y.-F. Han, *Appl. Catal. Environ.* **2021**, *298*, 120567.

[34] M. Singh, N. Kaur, A. Casotto, L. Sangaletti, N. Poli, E. Comini, *J. Mater. Chem. A* **2022**, *10*, 3178.

[35] K. R. B. Singh, S. Rathee, G. Nagpure, J. Singh, R. P. Singh, *Mater. Lett.* **2022**, *307*, 131092.

[36] S. M. Mane, A. R. Nimbalkar, J. S. Go, N. B. Patil, S. S. Dhasade, J. V. Thombare, A. S. Burungale, J. C. Shin, *Appl. Phys. A: Mater. Sci. Process.* **2021**, *127*, 13.

[37] S. Mallick, K. R. B. Singh, V. Nayak, J. Singh, R. P. Singh, *Mater. Lett.* **2022**, *306*, 130912.

[38] H. Beitollahi, S. Tajik, F. G. Nejad, M. Safaei, *J. Mater. Chem. B* **2020**, *8*, 5826.

[39] K. R. B. Singh, V. Nayak, J. Singh, A. K. Singh, R. P. Singh, *RSC Adv.* **2021**, *11*, 24722.

[40] L. J. A. Koster, O. Stenzel, S. D. Oosterhout, M. M. Wienk, V. Schmidt, R. A. J. Janssen, *Adv. Energy Mater.* **2013**, *3*, 615.

[41] S. Nandi, S. Kumar, A. Misra, *Mater. Adv.* **2021**, *2*, 6768.

[42] J. Park, S. Lee, J. Lee, K. Yong, *Adv. Mater.* **2013**, *25*, 6423.

[43] L. Upadhyaya, J. Singh, V. Agarwal, A. C. Pandey, S. P. Verma, P. Das, R. P. Tewari, *J. Polymer Research* **2014**, *21*, 550.

[44] V. B. Kumar, K. Kumar, A. Gedanken, P. Paik, *J. Mater. Chem. B* **2014**, *2*, 3956.

[45] P. Singh, K. R. B. Singh, J. Singh, P. Prasad, R. P. Singh, *RSC Adv.* **2021**, *11*, 25752.

[46] B. Panigrahy, M. Aslam, D. S. Misra, M. Ghosh, D. Bahadur, *Adv. Funct. Mater.* **2010**, *20*, 1161.

[47] G. Mamtmin, R. Abdurahman, Y. Yan, P. Nizamidin, A. Yimit, *Sens. Actuators, a* **2020**, *309*, 111918.

[48] S. Y. Park, B. J. Kim, K. Kim, M. S. Kang, K.-H. Lim, T. I. Lee, J. M. Myoung, H. K. Baik, J. H. Cho, Y. S. Kim, *Adv. Mater.* **2012**, *24*, 834.

[49] J. Luo, J. Lin, N. Zhang, X. Guo, L. Zhang, Y. Hu, Y. Lv, Y. Zhu, X. Liu, *J. Mater. Chem. C* **2018**, *6*, 5542.

[50] A. Serrà, P. Pip, E. Gómez, L. Philippe, *Appl. Catal. Environ.* **2020**, *268*, 118745.

[51] L. Upadhyaya, J. Singh, V. Agarwal, A. C. Pandey, S. P. Verma, P. Das, R. P. Tewari, *Process Biochem.* **2015**, *50*, 678.

[52] M. Skompska, K. Zarebska, *Electrochim. Acta* **2014**, *127*, 467.

[53] W. Li, M. Wu, H. Jiang, L. Yang, C. Liu, X. Gong, *Chem. Commun.* **2022**, *58*, 1910.

[54] S.-S. Lo, D. Huang, C.-H. Tu, D.-J. Jan, *J. Raman Spectrosc.* **2009**, *40*, 1694.

[55] H. Yuan, S. A. A. Aljneibi, J. Yuan, Y. Wang, H. Liu, J. Fang, C. Tang, X. Yan, H. Cai, Y. Gu, S. J. Pennycook, J. Tao, D. Zhao, *Adv. Mater.* **2019**, *31*, 1807161.

[56] Y. Guo, X. Wei, B. Wang, Y. Zhao, J. Min, W. Sang, *Phys. Status Solidi C* **2010**, *7*, 1577.

[57] H. Oh, J. Park, W. Choi, H. Kim, Y. Tchoe, A. Agrawal, G.-C. Yi, *Small* **2018**, *14*, 1800240.

[58] N. Islavath, *Sustainable Energy Fuels* **2020**, *4*, 863.

[59] S. Senapati, S. K. Srivastava, S. B. Singh, *Nanoscale* **2012**, *4*, 6604.

[60] P. Pawinrat, O. Mekasuwandumrong, J. Panpranot, *Cat. Com.* **2009**, *10*, 1380.

[61] U. K. Gautam, L. S. Panchakarla, B. Dierre, X. Fang, Y. Bando, T. Sekiguchi, A. Govindaraj, D. Golberg, C. N. R. Rao, *Adv. Funct. Mater.* **2009**, *19*, 131.

[62] J. B. In, H.-J. Kwon, D. Lee, S. H. Ko, C. P. Grigoropoulos, *Small* **2014**, *10*, 741.

[63] Z.-N. Ng, K.-Y. Chan, T. Tohsophon, *Appl. Surf. Sci.* **2012**, *258*, 9604.

[64] J. Elias, R. T. Zaera, C. L. Clément, *Thin Solid Films* **2007**, *515*, 8553.

[65] E. Navarrete, F. Güell, P. R. M. Alanis, E. Llobet, *J. Alloys Compd.* **2021**, *890*, 161923.

[66] P. Sengunthar, S. Patel, N. Thankachen, U. S. Joshi, *New J. Chem.* **2021**, *45*, 18853.

[67] D. Horwat, M. Mickan, W. Chamorro, *Phys. Status Solidi C* **2016**, *13*, 951.

[68] J. H. Zheng, Q. Jiang, J. S. Lian, *Appl. Surf. Sci.* **2011**, *257*, 5083.

[69] M. R. Alenezi, S. J. Henley, N. G. Emerson, S. R. P. Silva, *Nanoscale* **2014**, *6*, 235.

[70] P. X. Gao, C. S. Lao, W. L. Hughes, Z. L. Wang, *Chem. Phys. Lett.* **2005**, *408*, 174.

[71] J. Y. Lao, J. G. Wen, Z. F. Ren, *Nano Lett.* **2002**, *2*, 1287.

[72] J. G. Wen, J. Y. Lao, D. Z. Wang, T. M. Kyaw, Y. L. Foo, Z. F. Ren, *Chem. Phys. Lett.* **2003**, *372*, 717.

[73] B. Liu, H. C. Zeng, *Chem. Mater.* **2007**, *19*, 5824.

[74] Z. Dai, K. Liu, Y. Tang, X. Yang, J. Bao, J. Shen, *J. Mater. Chem.* **2008**, *18*, 1919.

[75] Y. Chen, Z. Wang, H. Fu, D. Han, F. Gu, *J. Mater. Chem. C* **2022**, *10*, 3318.

[76] H. Wang, L. Zhou, Y. Liu, F. Liu, X. Liang, F. Liu, Y. Gao, X. Yan, G. Lu, *Sens. Actuators B* **2020**, *305*, 127498.

[77] T. C. Damen, S. P. S. Porto, B. Tell, *Phys. Ther. Rev.* **1996**, *142*, 570.

[78] V. L. Patil, S. S. Kumbhar, S. A. Vanalakar, N. L. Tarwal, S. S. Mali, J. H. Kim, P. S. Patil, *New J. Chem.* **2018**, *42*, 13573.

[79] S. Gandhi, R. Kaur, V. Sharma, S. K. Mandal, *New J. Chem.* **2022**, *46*, 3645.

[80] S. A. Ansari, M. M. Khan, S. Kalathil, A. Nisar, J. Lee, M. H. Cho, *Nanoscale* **2013**, *5*, 9238.

[81] C. Sun, Y. Fu, Q. Wang, L. Xing, B. Liu, X. Xue, *RSC Adv.* **2016**, *6*, 87446.

[82] Z. Li, C. Lou, G. Lei, G. Lu, H. Pan, X. Liu, J. Zhang, *Sens. Actuators B* **2022**, *355*, 131347.

[83] S.-K. Min, H. Kim, Y. Noh, K.-S. Choi, S.-P. Chang, *Thin Solid Films* **2020**, *714*, 138249.

[84] J. Wang, J. Yang, N. Han, X. Zhou, S. Gong, J. Yang, P. Hu, Y. Chen, *Mater. Design* **2017**, *121*, 69.

[85] Z. Zhou, Y. Li, L. Liu, Y. Chen, S. B. Zhang, Z. Chen, *J. Phys. Chem. C* **2008**, *112*, 13926.

[86] N. L. Marana, V. M. Longo, E. Longo, J. B. L. Martins, J. R. Sambrano, *J. Phys. Chem. A* **2008**, *112*, 8958.

[87] L. Sponza, J. Goniakowski, C. Noguera, *Phys. Rev. B* **2016**, *93*, 195435.

[88] S. Xia, Y. Diao, C. Kan, *J. Colloid Interface Sci.* **2022**, *607*, 913.

[89] D. Vanmaekelbergh, L. L. van Vugt, *Nanoscale* **2011**, *3*, 2783.

[90] M. Isik, N. M. Gasanly, *Mater. Lett.* **2022**, *321*, 132415.

[91] M. N. H. Mia, M. F. Pervez, M. K. Hossain, M. R. Rahman, M. J. Uddin, M. A. A. Mashud, H. K. Ghosh, M. Hoq, *Result Phys* **2017**, *7*, 2683.

[92] P. R. Jubu, O. S. Obaseki, A. N. Abutu, F. K. Yam, Y. Yusof, M. B. Ochang, *Results in Optics* **2022**, *9*, 100273.

[93] M. K. Sikdar, G. Ghorai, T. R. Senapati, P. K. Sahoo, *J. Alloys Compd.* **2022**, *913*, 165179.

[94] R. V. Hariwal, H. K. Malik, A. Negi, A. Asokan, *Appl. Surf. Sci. Adv.* **2022**, *7*, 100189.

[95] S. Gea, S. A. Situmorang, N. Pasaribu, A. F. R. Piliang, B. Attaurrazaq, R. M. Sari, K. M. Pasaribu, S. Goutianos, *J. Mater. Res. Technol.* **2022**, *19*, 2730.

[96] H.-Q. Liu, C.-B. Yao, *Nanoscale* **2022**, *14*, 9169.

[97] S. Bang, S. Lee, T. Park, Y. Ko, S. Shin, S.-Y. Yim, H. Seo, H. Jeon, *J. Mater. Chem.* **2012**, *22*, 14141.

[98] M. K. Kavitha, H. John, P. Gopinath, R. Philip, *J. Mater. Chem. C* **2013**, *1*, 3669.

[99] J. Zhao, X. Yan, Y. Yang, Y. Huang, Y. Zhang, *Mater. Lett.* **2010**, *64*, 569.

[100] A. Kumawat, S. Chattopadhyay, K. P. Misra, R. D. K. Misra, P. Kumari, *Thin Solid Films* **2022**, *761*, 139521.

[101] W. W. Zhong, D. W. Guan, Y. L. Liu, L. Zhang, Y. P. Liu, Z. G. Li, W. P. Chen, *J. Nanomater.* **2012**, *2012*, 263679.

[102] Y. Zhang, C. Jia, Q. Kong, N. Fan, G. Chen, H. Guan, C. Dong, *ACS Appl. Mater. Interfaces* **2020**, *12*, 26161.

[103] S. Brahma, Y.-W. Yeh, J.-L. Huang, C.-P. Liu, *Appl. Surf. Sci.* **2021**, *564*, 150351.

[104] Q. Qi, T. Zhang, L. Liu, X. Zheng, Q. Yu, Y. Zeng, H. Yang, *Sens. Actuators B* **2008**, *134*, 166.

[105] C. Li, H. Zhou, S. Yang, L. Wei, Z. Han, Y. Zhang, H. Pan, *ACS Appl. Nano Mater.* **2019**, *2*, 6144.

[106] Y. Song, F. Gu, Z. Wang, D. Han, *ACS Appl. Nano Mater.* **2022**, *5*, 15298.

[107] D. Liu, X. Li, Y. Li, S. Yin, J. Liu, J. Zhang, A. C. S. Appl, *Nano Mater.* **2022**, *5*, 5745.

[108] P. Wang, T. Dong, C. Jia, P. Yang, *Sens. Actuators B* **2019**, *288*, 1.

[109] H. Du, W. Yang, W. Yi, Y. Sun, N. Yu, J. Wang, A. C. S. Appl, *Mater. Interfaces* **2020**, *12*, 23084.

[110] J. E. Lee, C. K. Lim, H. J. Park, H. Song, S.-Y. Choi, D.-S. Lee, A. C. S. Appl, *Mater. Interfaces* **2020**, *12*, 35688.

[111] L. Zhu, J. Wang, J. Liu, Z. Xu, M. S. Nasir, X. Chen, Z. Wang, S. Sun, Q. Ma, J. Liu, J. Feng, J. Liang, W. Yan, *Sens. Actuators B* **2022**, *354*, 131206.

[112] J. Liu, L. Zhang, B. Cheng, J. Fan, J. Yu, *J. Hazard. Mater.* **2021**, *413*, 125352.

[113] L. Jiang, S. Lv, W. Tang, L. Zhao, C. Wang, J. Wang, T. Wang, X. Guo, F. Liu, C. Wang, P. Sun, C. Zhang, J. Zheng, G. Lu, *Sens. Actuators B* **2021**, *345*, 130321.

[114] D. W. Kim, K. H. Park, S.-H. Lee, C. Fàbrega, J. D. Prades, J.-W. Jang, *J. Colloid Interface Sci.* **2021**, *582*, 658.

[115] R. Godbole, S. Ameen, U. T. Nakate, M. S. Akhtar, H.-S. Shin, *Mater. Lett.* **2019**, *254*, 398.

[116] V. S. Bhati, M. Kumar, R. Banerjee, *J. Mater. Chem. C* **2021**, *9*, 8776.

[117] K. Wu, W. Zhang, Z. Zheng, M. Debliquy, C. Zhang, *Appl. Surf. Sci.* **2022**, *585*, 152744.

[118] H. Tang, L. N. Sacco, S. Vollebregt, H. Ye, X. Fan, G. Zhang, *J. Mater. Chem. A* **2020**, *8*, 24943.

[119] X. Kang, S. Yip, Y. Meng, W. Wang, D. Li, C. Liu, J. C. Ho, *Nanoscale Adv.* **2021**, *3*, 6254.

[120] R. K. Mishra, G. J. Choi, Y. K. Mishra, A. Kaushik, Y. Sohn, S. H. Lee, J. S. Gwag, *J. Mater. Chem. C* **2021**, *9*, 7713.

[121] H.-P. Loock, P. D. Wentzell, *Sens. Actuators B* **2012**, *173*, 157.

[122] Y. Shi, H. Xu, T. Liu, S. Zeb, Y. Nie, Y. Zhao, C. Qin, X. Jiang, *Mater. Adv.* **2021**, *2*, 1530.

[123] L. Peng, Q. Zhao, D. Wang, J. Zhai, P. Wang, S. Pang, T. Xie, *Sens. Actuators B* **2009**, *136*, 80.

[124] X. Zheng, H. Fan, H. Wang, B. Yan, J. Ma, W. Wang, A. K. Yadav, W. Dong, S. Wang, *Ceram. Int.* **2020**, *46*, 27499.

[125] J. Ma, H. Fan, W. Zhang, J. Sui, C. Wang, M. Zhang, N. Zhao, A. K. Yadav, W. Wang, W. Dong, S. Wang, *Sens. Actuators B* **2020**, *305*, 127456.

[126] M. Siemons, U. Simon, *Sens. Actuators B* **2007**, *126*, 595.

[127] R. K. Mishra, S. B. Upadhyay, A. Kushwaha, T.-H. Kim, G. Murali, R. Verma, M. Srivastava, J. Singh, P. P. Sahay, S. H. Lee, *Nanoscale* **2015**, *7*, 11971.

[128] Y. J. Jeong, W.-T. Koo, J.-S. Jang, D.-H. Kim, M.-H. Kim, I.-D. Kim, *ACS Appl. Mater. Interfaces* **2018**, *10*, 2016.

[129] H. Nazemi, A. Joseph, J. Park, *Sens.* **2019**, *19*, 1285.

[130] E. Lee, Y. S. Yoon, D.-J. Kim, *ACS Sens.* **2018**, *3*, 2045.

[131] H.-J. Kim, J.-H. Lee, *Sens. Actuators B* **2014**, *192*, 607.

[132] Z. Li, H. Li, Z. Wu, M. Wang, J. Luo, H. Torun, P. Hu, C. Yang, M. Grundmann, X. Liu, Y. Fu, *Mater. Horiz.* **2019**, *6*, 470.

[133] Z. Li, Y. Huang, S. Zhang, W. Chen, Z. Kuang, D. Ao, W. Liu, Y. Fu, *J. Hazard. Mater.* **2015**, *300*, 167.

[134] H. Ji, W. Zeng, Y. Li, *Nanoscale* **2019**, *11*, 22664.

[135] Q. Wang, X. Cheng, Y. Wang, Y. Yang, Q. Su, J. Li, B. An, Y. Luo, Z. Wu, E. Xie, *Sens. Actuators B* **2022**, *355*, 131262.

[136] D. H. Kim, Y.-S. Shim, J.-M. Jeon, H. Y. Jeong, S. S. Park, Y.-W. Kim, J.-S. Kim, J.-H. Lee, H. W. Jang, *ACS Appl. Mater. Interfaces* **2014**, *6*, 14779.

[137] W. Ge, S. Jiao, Z. Chang, X. He, Y. Li, *ACS Appl. Mater. Interfaces* **2020**, *12*, 13200.

[138] A. A. Baharuddin, B. C. Ang, A. S. M. A. Haseeb, Y. C. Wong, Y. H. Wong, *Mater. Sci. Semicond. Process.* **2019**, *103*, 104616.

[139] C. Wang, J. Zhu, S. Liang, H. Bi, Q. Han, X. Liu, X. Wang, *J. Mater. Chem. A* **2014**, *2*, 18635.

[140] J. Huang, Y. Dai, C. Gu, Y. Sun, J. Liu, *J. Alloys Compd.* **2013**, *575*, 115.

[141] L. Wang, Y. Kang, Y. Wang, B. Zhu, S. Zhang, W. Huang, S. Wang, *Mater. Sci. Eng. C* **2012**, *32*, 2079.

[142] Y. Zheng, L. Zheng, Y. Zhan, X. Lin, Q. Zheng, K. Wei, *Inorg. Chem.* **2007**, *46*, 6980.

[143] L. Lv, P. Cheng, Y. Zhang, Y. Zhang, Z. Lei, Y. Wang, L. Xu, Z. Weng, C. Li, *Sens. Actuators B* **2022**, *358*, 131490.